International Journal of Automotive Technology, Vol. 19, No. 5, pp. 869–878 (2018)
DOI 10.1007/s12239–018–0084–2

pISSN 1229–9138/ eISSN 1976–3832

RANGE EXTENDER MODULE TRANSMISSION TOPOLOGY STUDY

Konrad Herold[1)], Marius Böhmer[1)], Rene Savelsberg[1)], Alexander Müller[1)], Jan Schröter[2)], Jan Karthaus[3)], Un-Jae Seo[3)], Georg Jacbos[2)], Kay Hameyer[3)] and Jakob Andert[4)*]

[1)]Institute for Combustion Engines (VKA), RWTH Aachen University, Aachen 52074, Germany
[2)]Institute for Machine Elements and Machine Design (IME), RWTH Aachen University, Aachen 52062, Germany
[3)]Institute of Electrical Machines (IEM), RWTH Aachen University, Aachen 52062, Germany
[4)]Mechatronic Systems for Combustion Engines (MSCE), RWTH Aachen University, Aachen 52074, Germany

(Received 7 February 2017; Revised 7 September 2017; Accepted 17 March 2018)

ABSTRACT–Range extender modules are one option to compensate for short drive ranges of electric vehicles. The close interaction of combustion engine and generator poses new challenges in development. A key requirement for range extender systems is to be light and virtually imperceptible in operation. High-speed electrical machines aim at increasing power density. However, their introduction in a range extender requires a gearbox. The combustion engine torque fluctuations can lead to rattle in the gearbox. The rattle can be overcome by a dual mass flywheel. An interdisciplinary model is developed and used to analyse three different range extender systems: one with a low speed generator without gearbox, one with a high-speed generator, and one with a high-speed generator and a dual mass flywheel. The efficiency was found to be higher for the system with a low speed generator, whereas the power density and the costs are beneficial for the high-speed concept. A dual mass flywheel eliminates the changes of torque direction in the gearbox. It reduces the speed fluctuations of the gearbox and generator by over 90 % compared to the low speed setup. But it increases rolling moment and subsequently chassis excitation compared to a setup with only a gearbox.

KEY WORDS : Range extender, Electric generator, Combustion engine, Gearbox, Dual mass flywheel, Speed fluctuations, Efficiency, NVH

NOMENCLATURE

c	: spring constant, Nm/rad
d	: damping constant, Nm/rad/s
i	: current, A
J	: mass inertia, kg/m^2
L	: inductance, H
n	: rotational speed, 1/min
P	: power, W
p	: number of pole pairs, 1
r	: radius, m
R	: resistance, Ω
T	: torque, Nm
u	: voltage, V
v	: velocity, m/s
θ	: phase angle, rad
ρ	: density, kg/m^3
σ	: stress, N/m^2
τ	: time constant, s
Ψ	: magnetic flux linkage, Vs
ψ	: angle, rad
ω	: angular velocity, rad/s

SUBSCRIPTS

I, II	: primary/secondary side
a, b, c	: phase quantities in the three phase system
B	: combustion
CD	: combustion duration
CS	: combustion start
d	: direct axis
DMF	: dual mass flywheel
el	: electrical
F	: permanent magnet excitation
GB	: gear box
i	: current control loop
ICE	: Internal combustion engine
max	: maximum value
n	: nominal value
R	: radial
s	: stator domain
ST	: connecting rod
T	: tangential
tot	: total
PMSM	: permanent magnet synchronous machine
q	: quadrature axis
red	: reduced

**Corresponding author.* e-mail: andert@vka.rwth-aachen.de

1. INTRODUCTION

Electric vehicles are an important technology for sustainable mobility. Fleet emission regulation and rising awareness put pressure on OEMs to introduce electric vehicles to the market. Until now, the market penetration of electric vehicles has not met the desired level, as electric vehicles do not fulfill all user requirements. Herrmann and Matthé (2014) stated that 72 % of car journeys from and to work in the US are less than 67 km. Eberle (2012) showed that 80 % of the daily car journeys in Germany are less than 50 km. Today's electric vehicle technology is capable of covering such distances. For longer distances, either the battery size has to be increased or a range extender has to be used. As a relatively small battery can cover most journeys, a larger battery would lead to excessive weight, which would then increase the energy consumption.

A range extender is much cheaper and lighter than a large battery and it can be refueled significantly faster than a battery could be charged. Heron and Rinderknecht (2013) give an overview over possible range extender topologies. Efficiency, weight, packaging, and cost are named as important design criteria, which have to be weighted for each specific application. Currently, the gasoline engine is the most promising technology. A gasoline engine is a comparatively cheap technology and all components are readily available in automotive quality at competitive prices. Examples of range extenders based on gasoline engines are shown in Andert *et al*. (2012), Bassett *et al*. (2012) and Fischer *et al*. (2009).

Very strong interdependencies of the subsystems combustion engine, dual-mass fly-wheel, transmission, electric motor and frequency inverter, and comprehensive control are the most challenging part of this research. To solve this conflict, different chairs of mechanical and electrical engineering of the mobilEM research training group are working together and combining their key competencies to setup an innovative Co-Simulation approach. The Co-Simulation environment combines the different mechanical, electrical, and control domains to one simulation model.

This paper starts with an analysis of all subsystems of a range extender. The models, except for the dual-mass fly-wheel (DMF), are derived from existing and tested components. In the following chapter, the electrical machine is studied. The third chapter covers the thermodynamic and mechanical model of the combustion engines. The fourth chapter explains the gearbox model. In the fifth chapter, the dual mass flywheel (DMF) is introduced. Chapter six shows the integration of the simulation model and the simulation results. This paper is concluded in the seventh chapter.

2. ELECTRICAL MACHINE

A range extender system requires an electrical machine as generator and a starter, which has a high efficiency, high electric power density, and a compact design. The electrical machine is used mostly as a generator. The requirements for use as a starter are discussed by Gebrehiwot and van den Bossche (2015). High power densities, thus a smaller machine space and less weight, can be achieved with permanent magnet synchronous machines (PMSM). For high-speed applications, embedded permanent magnets within the rotor are used as excitation. The design methodology of the electrical high-speed machines, which is discussed in the following section, requires particular attention.

2.1. High-speed Electrical Machines

The key advantage of electrical high-speed machines is their high power density. By increasing the required speed of a machine, the required volume is decreased. Possible machine topologies are synchronous machines with separate excitation or self-excitation with permanent magnets, squirrel cage induction machines, or reluctance machines. Very high machine efficiencies can be reached by using PMSM (Borisavljevic *et al*., 2010).

Although there are lots of advantages for high-speed PMSM, there are some disadvantages such as higher design costs, higher iron losses, and mechanical friction losses as well (Bianchi *et al*., 2003). In addition, high stresses due to centrifugal forces, which are dependent on the speed and radius, require particular attention to the mechanical component strength of the rotor:

$$\sigma_T \propto \rho v^2 = \rho(2\pi r n)^2 \tag{1}$$

where σ_T is the tangential stress component, ρ the density, v the circumferential speed, r the radius, and n the speed of the rotor. Within the design of electrical machines, it is important not to reach mechanical stresses, which are higher than the yield strength of the stack lamination material. Mechanical stresses above the yield strength of the electrical steel sheet material can cause plastic deformation within the stack lamination, which influences the machine's operating behavior and its lifetime, and it can lead to cracks within the stack lamination and ultimately

Table 1. Machine specifications.

Description	Parameter/ Unit	LS-PMSM	HS-PMSM
Nominal speed	n_n/min^{-1}	3000	10000
Maximum speed	n_{max}/min^{-1}	10000	25000
Nominal torque	T_n/Nm	100	29
Nominal power	P_n/kW	30	30
Number of pole pairs	p	3	3
Estimated active mass	m/kg	20.9	14.3
Estimated frame volume	V/l	5.8	3.9

destruction of the rotor (Karthaus *et al*., 2017).

For the study of the range extender drive train model, two different machines are considered: The low-speed machine (LS-PMSM) is used for the gearless operation of the range extender. In contrast to the LS-PMSM, a gearbox is required to operate the range extender with the high-speed machine (HS-PMSM).

For the following study, two of-the-shelf electric machines are compared. The machine models are based on data from (Grosse *et al*., 2014). Improved results could be achieved with use-case specific designs. As range extenders have to be fitted into already costly electric vehicles, a custom design was omitted as the authors expect a series production with already industrialized components. In Table 1, the used machines' specifications are listed.

The active mass of the electric machines is defined as the mass of the iron parts and copper windings. The magnets are considered to have the same density as iron for this estimation.

2.2. Specifications of Electrical Machines

Both machines use a v-shaped embedded permanent magnet system as shown in Figure 1. When compared to other arrangements of the rotor magnets, this topology leads to low losses in the permanent magnets, and therefore high efficiencies can be obtained (Finken *et al*., 2010).

2.3. Electrical Machine Control for Drive Train Model

2.3.1. Basic PMSM model

The machine model equations can be derived from the general vectorial voltage equation of the three phase system:

$$\begin{pmatrix} u_a \\ u_b \\ u_c \end{pmatrix} = \mathbf{R}_s \cdot \begin{pmatrix} i_a \\ i_b \\ i_c \end{pmatrix} + \frac{\mathrm{d}}{\mathrm{d}t} \begin{pmatrix} \Psi_a \\ \Psi_b \\ \Psi_c \end{pmatrix}, \tag{2}$$

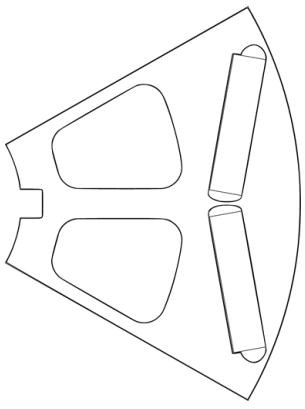

Figure 1. Rotor geometry (Grosse *et al.*, 2014).

with

$$\mathbf{R}_s = \mathbf{I} R_l, \tag{3}$$

where $\mathbf{I}$ is the identity matrix, Ψ is the flux linkage in each phase, R_l is the stator resistance, u the voltage, and i the current in phase a, b, and c, respectively. The dq-transformation changes the machine model into the rotating coordinate system:

$$\begin{pmatrix} u_d \\ u_q \end{pmatrix} = R_l \begin{pmatrix} i_d \\ i_q \end{pmatrix} + \begin{pmatrix} L_d \dfrac{\mathrm{d}i_d}{\mathrm{d}t} \\ L_q \dfrac{\mathrm{d}i_q}{\mathrm{d}t} \end{pmatrix} + \omega_{el} \begin{pmatrix} L_q i_q \\ \Psi_F + L_d i_d \end{pmatrix}, \tag{4}$$

where L_d is the inductance in d-axis, and L_q is the inductance in q-axis. i_d and i_q are the currents in the rotor synchronous frame. Ψ_F is the excitation flux linkage. ω_{el} is the radial electrical speed described by

$$\omega_{el} = p \cdot \omega_{mech}. \tag{5}$$

where p is the number of pole pairs of the electrical machine and ω_{mech} is the mechanical speed of the rotor. For the derivation of torque produced by the machine, the transmitted air gap power P is calculated by multiplying currents and induced voltages (Schröder, 2015):

$$P = \frac{3}{2}\left[-i_d \omega_{el} L_q i_q + i_q \omega_{el}\left(\Psi_F + L_d i_d\right)\right]. \tag{6}$$

The factor $\frac{3}{2}$ compensates the amplitude adjustment used in the transformation of the three phase quantities. Then, the resulting torque can be described by

$$T_{el} = \frac{P \cdot p}{\omega_{el}} = \frac{3}{2} p\left[\Psi_F i_q + (L_d - L_q) i_d i_q\right]. \tag{7}$$

2.3.2. Currents control of the PMSM

The inverter converts the supplied dc voltage into the desired ac voltage to control the electric motor. The dc voltage is either directly determined by the battery or it is supplied by a dc/dc converter.

The control of the rotating speed of the generator is realized by controlling the generator torque. The reference d- and q-axis current are generated by computing the required torque for a given speed reference. A proper control of the quasi dc d- and q-axis current can be realized by conventional proportional plus integral (PI) controllers. The d- and q-axis current set points are determined by the maximum torque per ampere (MTPA) function. The MTPA function maximizes the torque output for a given overall stator current i_s The block diagram of a drive system incorporating speed control, current vector control, and flux-weakening control is shown in Figure 2.

The given reference current i_s can be divided into two components:

$$\begin{pmatrix} i_{\mathrm{d}}' \\ i_{\mathrm{q}}' \end{pmatrix} = \begin{pmatrix} i_{\mathrm{s}}^{*} \sin(\gamma) \\ i_{\mathrm{s}}^{*} \cos(\gamma) \end{pmatrix} \tag{8}$$

where γ is the angle between q-axis and the current angle in the positive direction. At any given reference current, can be differentiated mathematically with respect to γ to find the γ^{*} which yields the maximum torque:

$$\gamma^{*} = \sin^{-1}\left(\frac{-\psi_{\mathrm{F}} + \sqrt{\psi_{\mathrm{F}}^{2} + 8(i_{\mathrm{s}}^{*})^{2}(L_{\mathrm{d}} - L_{\mathrm{q}})^{2}}}{4 i_{\mathrm{s}}^{*}(L_{\mathrm{q}} - L_{\mathrm{d}})} \right). \tag{9}$$

The maximum torque for given reference current can be obtained while the drive operating point can be maintained within the voltage limitation. The flux weakening control is accomplished above the base speed of the generator, which is limited by the inverter voltage. Here, the dc control is accomplished when the generator voltage exceeds the voltage limitation. A flux weakening angle is obtained by the standard PI voltage feedback loop. For a given reference of i_{d} and i_{q}, a classical anti-wind up method, which prevents the integration of the PI controller in saturation, is used as the current regulator. The dynamics of the current can be expressed as:

$$\begin{pmatrix} i_{\mathrm{d}} \\ i_{\mathrm{q}} \end{pmatrix} = \frac{1}{1+\tau_{\mathrm{i}} s} \begin{pmatrix} i_{\mathrm{d}}^{*} \\ i_{\mathrm{q}}^{*} \end{pmatrix} - \frac{\tau_{\mathrm{i}}}{1+\tau_{\mathrm{i}} s} \begin{pmatrix} \dfrac{\Delta u_{\mathrm{d}}}{L_{\mathrm{d}}} \\ \dfrac{\Delta u_{\mathrm{q}}}{L_{\mathrm{q}}} \end{pmatrix}, \tag{10}$$

where τ_{i} is a time constant determining the bandwidth of the current closed loop. s is the Laplace frequency operator. Δu_{d} and Δu_{q} are voltage differences defined as

$$\begin{pmatrix} \Delta u_{\mathrm{d}} \\ \Delta u_{\mathrm{q}} \end{pmatrix} = \begin{pmatrix} u_{\mathrm{d}}' - u_{\mathrm{d}}^{*} \\ u_{\mathrm{q}}' - u_{\mathrm{q}}^{*} \end{pmatrix} \tag{11}$$

where u'_{d} and u'_{q} are the unmodulated voltages, whereas. u^{*}_{d} and u^{*}_{q} are the modulated voltages. The overmodulation strategy is applied to achieve a stable operation in the field weakening region (Liu and Hameyer, 2016):

$$u_{\mathrm{d,k}}^{*} = \begin{cases} u_{\mathrm{d,k}}' & \text{if } \mathrm{sign}(u_{\mathrm{d,k}}' i_{\mathrm{q,k}}) > 0 \\ \mathrm{sign}(u_{\mathrm{d,k}}') \sqrt{u_{\max}^{2} - u_{\mathrm{q,k}}^{*2}} & \text{otherwise} \end{cases}, \tag{12}$$

$$u_{\mathrm{q,k}}^{*} = \begin{cases} \mathrm{sign}(u_{\mathrm{q,k}}') \sqrt{u_{\max}^{2} - u_{\mathrm{d,k}}^{*2}} & \text{if } \mathrm{sign}(u_{\mathrm{q,k}}' i_{\mathrm{q,k}}) > 0 \\ u_{\mathrm{q,k}}' & \text{otherwise} \end{cases}, \tag{13}$$

where $u_{\max}$ is the voltage limitation and the subscript k denotes sampling step.

3. COMBUSTION ENGINE MODEL

In the following sections, the thermodynamic and mechanic modelling of the engine is described. The model is derived from the range extender engine described in Andert *et al.* (2012) and Köhler *et al.* (2012). The specifications are listed in Table 2.

The torque output is a product of the pressure in the combustion chamber and the cranktrain geometry. The pressure acting on the piston is converted to torque via the cranktrain kinematics. The kinematics depend on the cranktrain design (i.e. connecting rod ratio) and the current cranktrain position.

3.1. Thermodynamic Model

The pressure inside a combustion chamber depends on

Table 2. Characteristics of the combustion engine (An-dert *et al.*, 2012).

Description	Parameter/Unit	Value
Layout		Four-stroke, two cylinder, 90°-V, fuel port injection
Displacement	V_{h}/l	0.799
Bore	d/mm	80
Stroke	s/mm	79.5
Nominal power	P/kW	30

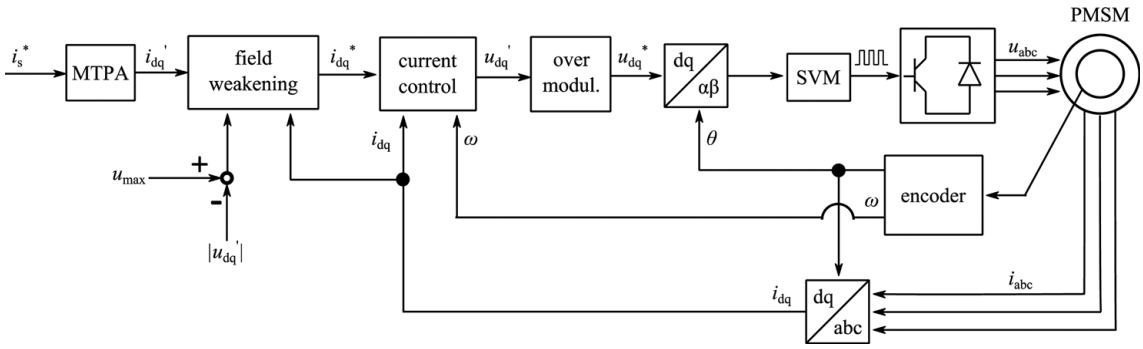

Figure 2. Control of the PMSM (Liu and Hameyer, 2016).

many factors. Four phases have to be separated:
– Intake of fresh charge
– Compression and expansion
– Combustion
– Exhaust of burnt mixture

The different phases of the 4-stroke Otto cycle will be described in the following. The model is always a single-zone model.

During the intake of the fresh charge, the properties of the mixture are assumed to be the same as in the intake manifold. Throttling losses are modeled depending on the load request by assuming a cylinder pressure below atmospheric pressure during the intake stroke.

During compression and expansion, the thermodynamic properties of ideal gases are used. The compression is assumed polytropic, with a coefficient of 1.35. During expansion, the polytropic coefficient is reduced to 1.3 to account for the three-atom molecules of the burnt mixture. The polytropic coefficients are lower than the isentropic coefficients. This takes deviations from isentropic changes of state into account, e.g. non-reversibility.

The vibe approach (Vibe, 1970) is chosen to model the heat addition during the combustion phase. The heat added at a specific crank angle is described with the following formula:

$$\frac{\mathrm{d}Q_\mathrm{B}}{\mathrm{d}\varphi} = \frac{\mathrm{d}Q_\mathrm{B,tot}}{\mathrm{d}\varphi} \cdot 6.908 \cdot (m+1) \cdot \left(\frac{\varphi-\varphi_\mathrm{CS}}{\Delta\varphi_\mathrm{CD}}\right)^m \cdot \exp\left[-6.908 \cdot \left(\frac{\varphi-\varphi_\mathrm{CS}}{\Delta\varphi_\mathrm{CD}}\right)^{m+1}\right], \quad (14)$$

where φ is the current crank angle, φ_CS is the crank angle at combustion start, and φ_CD represents the duration of the heat addition in crank angle domain. Q_B is the heat added to the cylinder, and $Q_\mathrm{B,tot}$ is the total heat added during combustion. The factor of 6.908 ensures that 99.9 % of $Q_\mathrm{B,tot}$ is released after the φ_CD angle change. m is the form number of the combustion. A small value of m stands for a heat addition rate peak at the beginning of the combustion, while a high value stands for a peak at the end. For the following studies, a form number of 2 is chosen. This corresponds to the maximum burn rate in the middle of the combustion event (Pischinger *et al*., 2009).

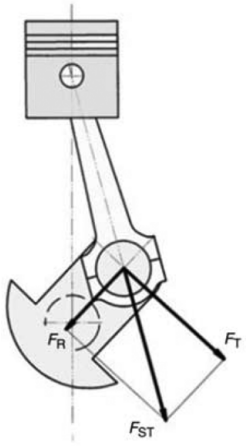

Figure 3. Forces acting on the crankpin (van Basshuysen and Schäfer, 2015).

To account for wall heat losses and other losses, an empirical loss from chemical fuel enthalpy to heat addition is introduced.

During the exhaust stroke, the pressure is set to the exhaust manifold pressure. The cylinder pressure is ramped down to the exhaust manifold pressure during the outlet valve opening. This corresponds to chocked flow across the exhaust valve orifice, which cannot balance the pressures instantaneously. The thermodynamical parameters are obtained by fitting the simulated pressure over crank angle to measurements of the cylinder pressure. The measurments are conducted on the engine presented in Andert *et al*. (2012) and Köhler *et al*. (2012).

3.2. Crank Train Model

The gas force acting on the piston is transferred to the cranktrain. As the connecting rod is mechanically a compression strut, it is limited to transmitting forces in the connecting line of the bearings. The gas forces and inertia forces of the piston are parallel to the cylinder bore axis. If the connecting rod is not aligned with the cylinder bore axis, the force component perpendicular to the cylinder bore is compensated by the normal force of the piston. The normal force increases the friction of the piston on the cylinder wall. A schematic of a cranktrain is shown in Figure 3.

The connecting rod force F_ST can be divided into two components:
– A radial component F_R in crankshaft domain and
– A tangential component F_T in crankshaft domain.

The radial force does not contribute to the crankshaft torque. Only the tangential component defines the crankshaft torque. Based on the crankshaft pin radius and

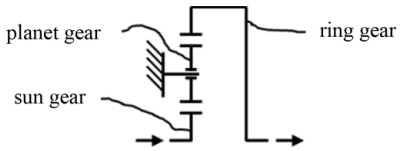

Figure 4. Architecture of the transmission.

Table 3. Characteristics of the transmission.

Transmission	n_max / min^{-1}	P_cont/kW	i	m/kg	V/l
Original	20,000	20	– 4.6	5,42	1,23
Adjusted	25,000	30	– 4.6	5,42	1,23

the connecting rod length, the torque output can be computed.

Two inertias model the cranktrain dynamics: the translational mass of the connecting rod and the piston as well as the inertia of the rotating part of the connecting rod and the crankshaft. The translational inertia force is imposed on the piston together with the gas force.

The rotational inertia torque is added to the combustion engines output torque. The friction is accounted for by an average friction torque, which is imposed on the cranktrain regardless of crankshaft position.

4. GEARBOX MODEL

For the high speed concept, a transmission consisting of one planetary gear stage with three planetary gears and a ratio of − 4.6 is utilized.

The sun gear is connected to the electrical machine and is therefore applied with a maximum rotational speed of 20,000 min^{-1}. The transmission was originally developed for a high speed electrical drive for mobile machinery (Schröter *et al*., 2015). Nevertheless, it can be used in this range extender concept, because its architecture (Figure 4) is advantageous for high rotational speed.

Since the planet carrier is fixed, no paddling losses of the carrier occur and no centrifugal loads act upon the planet bearing. A helical gearing is chosen in order to achieve a high running smoothness. For all gear wheels, roller bearings are used. Radial shaft seals are used for the dynamic sealing locations. Further details for the transmission's design are described in Schröter and Jacobs (2014). The transmission's characteristics are listed in Table 3. The gearbox mass refers to the active parts, such as shafts and gears. The housing, bearing and seals were neglected as their masses strongly depend on the integration level of the components.

The transmission's efficiency map was measured in Schröter *et al*. (2014). Losses of all bearings, seals, gear meshing, and the injection lubrication are included. Efficiency reaches 98.1 % in the full load range at low rotational speed (5,000 min^{-1}) and 96.2 % in the full load range at high speed (20,000 min^{-1}).

For the simulation model, this measured efficiency map is scaled from 20 kW to 30 kW using FEV TopExpert FACE.

The efficiency map's deviation is 0.3 % at maximum torque and increases towards lower torque. At ten percent of maximum torque, the deviation is at 3.0 %.

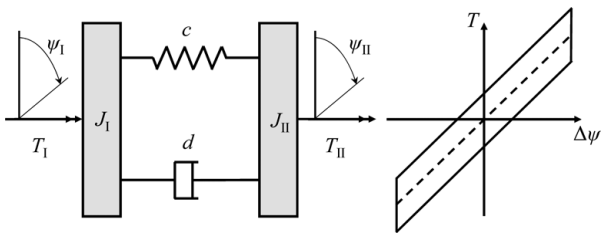

Figure 5. Architecture and hysteresis curve of the DMF.

Table 4. Characteristics of the DMF.

Description	Parameter/Unit	Value
Primary mass inertia	J_I/kgm^2	0.0074
Secondary mass inertia	J_{II}/kgm^2	0.0067
Spring constant	c/(Nm/rad)	53.7
Damping constant	d/(Nm/rad/s)	0.147

5. DUAL-MASS FLY-WHEEL MODEL

Dual-mass fly-wheels (DMF) are a state of the art technology to reduce speed fluctuations in a drivetrain (van Basshuysen and Schäfer, 2015). A DMF splits the drivetrain into two parts. The primary and secondary side are usually connected by an arc spring. If the parameters are chosen correctly, the system's resonance frequency lies below the idle speed of the engine. The drivetrain is then operated overcritically, which leads to a decoupling of the primary and secondary side. The torque and speed fluctuations are significantly reduced on the secondary side. As a result, gear rattle is virtually eliminated and the stress acting on the gear decreases (Reik *et al*., 1998).

Damping is caused by friction between the arc spring and the case. The spring rate and friction coefficient are non-constant, as dynamic forces act on the spring and the spring usually has a clearance.

To model the nonlinear characteristics, the arc spring can be discretized into mass and spring elements as proposed by Stier *et al*. (2009). The friction is calculated using the sum of the centrifugal force and the spring force normal to the case. The variation losses and the changing magnifying function are reproduced as a function of rotational speed.

The DMF-model used in the following is a linear model similar to Walter *et al*. (2007) and clearance is neglected. A schematic of the model is shown in Figure 5. Friction is modeled by the damping constant d, and the spring constant is c. The inertias of the combustion eninge and generator side are J_I and J_{II} respectively. With the

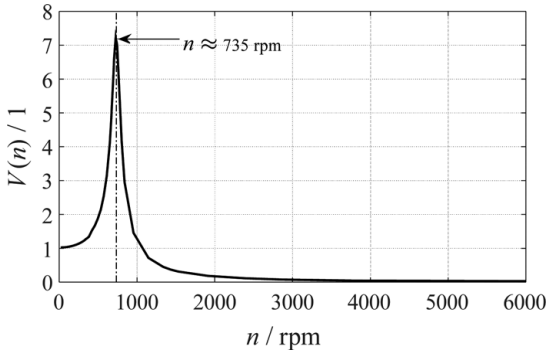

Figure 6. Magnifying function of the secondary side.

simplified model, it is possible to evaluate potentials of a DMF in a range extender application, whilst the parameter numbers and compuatational effort stay low. The DMF is designed for overcritical operation. Table 4 shows the parameters used for the simulations.

Figure 6 shows the magnifying function of the rotational acceleration on the secondary side as a function of the engine speed.

The dampened natural frequency is equivalent to ca. 735 min^{-1} engine speed. In the operation speed range, the system is supercritical and the secondary side is sufficiently isolated from the engine's excitation.

6. CO-SIMULATION

In this section, the overall simulation model is described. The effect of a high speed generator on the efficiency is investigated. As a further aspect, the influence of a dual-mass flywheel on gear excitation and vehicle body excitation is analyzed.

6.1. Simulation Model

The system layout is shown in . The component models are described in the previous chapters. All component models are derived from existing components which were chosen to harmonize in terms of speed, torque and power. The models were validated individually, as described in the respective chapters. Only the DMF model was derived from literature.

MATLAB/Simulink is used for the simulation. All component subsystems are interconnected using the SimDriveLine physical blockset. The combustion engine and generator torque are calculated in the respective model and exerted on the shafts. The gearbox and the dual mass flywheel are entirely modeled with the physical blockset.

The gearbox efficiency is introduced with an equivalent map based loss torque. The rotational speed calculated by the mechanical subsystem is the input to the combustion engine and the electrical machine. The torque is controlled by the combustion engine. The electrical machine operates in speed control mode. This research focuses on two operating points. The aim is to compare range extender topologies. Implications of the topologies on driving cycles can be studied in future research.

6.2. Influence on Efficiency

In this paragraph, the effect of equipping a range extender with a low or high speed generator is evaluated. If the range extender uses a low speed generator, no gearbox is used. For a high speed generator, a gearbox is used to reduce the generator speed level to the combustion engine speed level. The study was carried out for two operating points: the point of optimum brake specific fuel consumption (ICE: 3,000 min^{-1}/55 Nm; abbreviation OB) and the maximum power point (ICE: 4,500 min^{-1}/50 Nm; abbreviation MP). The efficiencies for the combustion engine (ICE), the gearbox (GB), and the dual mass flywheel (DMF) are stated in Table 5. The efficiencies are averaged over 720° crank angle to eliminate all cyclic influences on the efficiency calculation.

The low speed setup does not have gearbox losses,

Table 5. Efficiency impact of low speed and high speed generator.

EM	Power train		η_{ICE}/%	η_{DMF}/%	η_{GB}/%	η_{GEN}/%	η_{tot}/%
LS	-	OB	29.95	-	-	95.92	28.73
HS	GB	OB	29.16	-	96.70	93.93	26.49
HS	GB+ DMF	OB	29.20	99.95	96.71	94.40	26.64
LS	-	MP	27.47	-	-	96.50	26.51
HS	GB	MP	27.46	-	96.38	90.27	23.89
HS	GB+ DMF	MP	27.49	~ 100	96.38	90.47	23.97

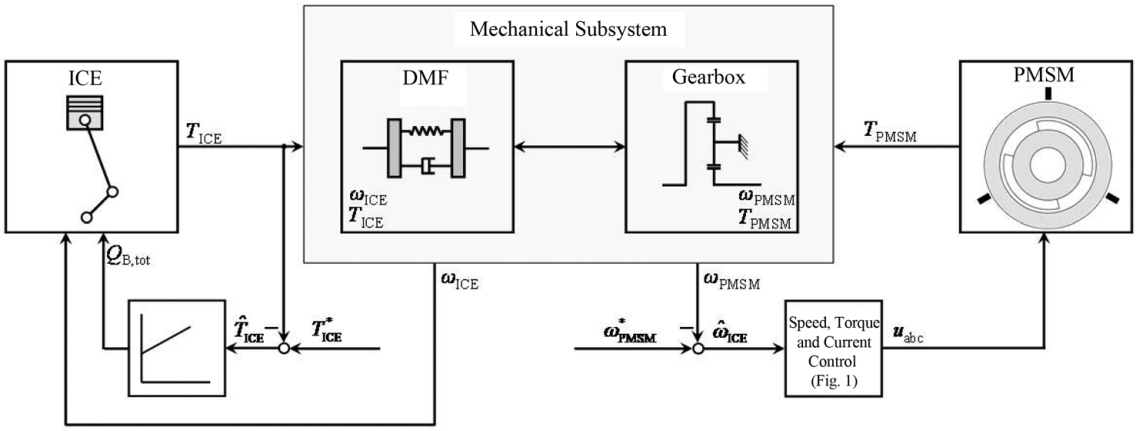

Figure 7. Component interaction and controllers used in the simulation model.

whereas the high speed setup suffers from gearbox losses. In order to improve the system efficiency for the range extender system, the gain in electric machine efficiency would have to overcompensate the gearbox losses. As can be seen in Table 5, the total efficiency decreases by 2.1 percentage points at the optimum break specicifc fuel consumption point and decreases by 2.5 percentage points at the maximum power point when switching from a low speed to a high speed generator.

This is caused by the lower efficiency of the HS-PMSM and the gear losses, while the DMF's impact on efficiency is negligible.

The efficiency of the high speed and low speed generator is comparable for the OB operating point. For the MP operating point with higher speed, the iron losses increase in the high speed machine. This leads to an efficiency decrease of about 4 %. If the electrical machine was specifically designed for this application it would provide an essentially higher efficiency for this operating point.

6.3. System Comparison

Switching from a high speed generator with a gearbox to a low speed generator does not only influence the system efficiency. As a high speed generator has a higher power density, the cost for active magnet material and the machine weight can be reduced.

Table 6 shows the comparison of the high speed and the low speed concept regarding the total efficiency, the volume and mass. The high-speed concept offers a lower efficiency, whereas the total volume could be decreased by 11.6 % and the mass by 5.6 %. Therefore, the total system weight is lower and the mass of the cost intensive materials, such as permanent magnets (decrease of 28.4 %) and copper (decrease of 55.3 %) is reduced further.

Table 6. System comparison regarding total efficiency, volume and mass.

Concept	η_{tot}/%	V_{tot}/l	m_{tot}/kg
LS	28.73	5.8	20.9
HS	26.49	5.13	19.72

Table 7. Speed fluctuations of the different power trains.

EM	Power train		d_{em}/%	d_{ice}/%
LS	-	OB	6.037	
HS	GB	OB	3.200	
HS	GB+TMF	OB	0.126	10.936
LS	-	MP	2.847	
HS	GB	MP	1.383	
HS	GB+TMF	MP	0.026	4.919

By a highly integrated design, the benefit for both weight and volume can be improved even more.

6.4. Influence on Speed Fluctuation

The speed fluctuation refers to the relative difference from minimum to maximum speed of a component. The speed fluctuation of the range extender system is given in Table 7 for the different setups. It decreases when switching from a low speed generator to a high-speed generator with a gearbox, as the high-speed system has a higher reduced inertia. The DMF further reduces the speed fluctuations on the secondary side as intended. The speed fluctuations on the primary side increase, as the DMF decouples the high secondary inertia from the low primary inertia.

As the gearbox changes the direction of motion, the rolling moment of the generator and the combustion engine interfere destructively. This corresponds to the solid line in Figure 8. If the DMF is introduced to the system, the rigid link between combustion engine and generator side is replaced by a spring. This allows the two inertias to accelerate independently. Subsequently, the destructive interference of inertia torques is not present anymore. The rolling moment increases, as shown in the dashed line in Figure 8. This leads to an increased excitation of the vehicle body.

It is important to look at the load situation in the gearbox

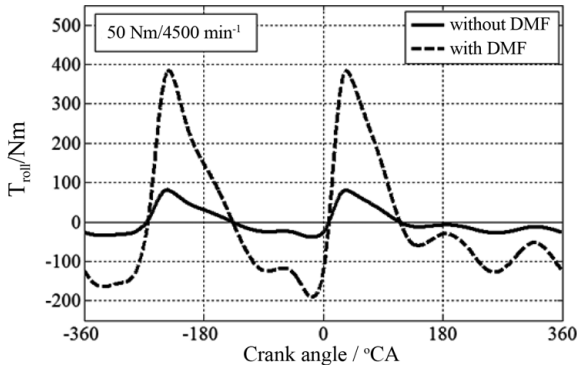

Figure 8. Influence of the DMF on the rolling moment.

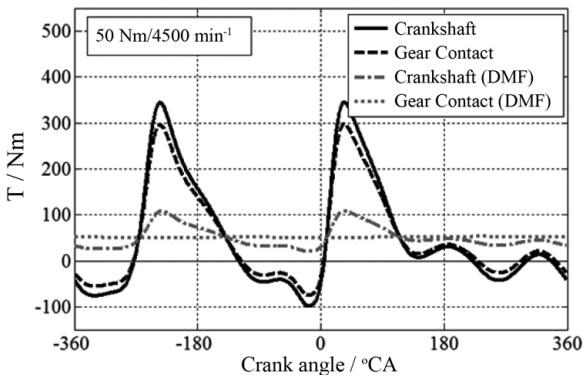

Figure 9. Influence of the DMF on the torque acting on the crankshaft and the gear contact.

to evaluate the danger of gear rattle. Figure 9 shows the load acting on the gear contact over 720° CA. The solid line shows the torque on the connection flange between the combustion engine and the gearbox without DMF. The dashed line shows the torque in the gear contact without DMF. The gears change their active flanks back and forth, as the torque changes its sign, which causes gear rattle. The gray dot-dashed line in Figure 9 shows the torque on the connection between ICE and gearbox with DMF. The DMF reduces the torque fluctuations at this point as the accelerations and deceleration of the crankshaft increase. The grey dotted line shows the gear contact torque with DMF. The gear contact torque does not change its sign. The DMF helps to eliminate the gear rattle. An approach to avoid gear contact torque sign changes while eliminating the rolling torque is discussed in Pischinger and Andert (2014) and Andert *et al*. (2017).

7. CONCLUSION

An interdisciplinary simulation model for a range extender consisting of a V2-internal combustion engine, a dual mass flywheel, a gearbox, and a permanent magnet synchronous machine has been developed.

Using this model, the efficiency and speed fluctuations for different range extender system configurations and operating points were evaluated. The optimal system design is a tradeoff between efficiency and power density. The total efficiency is the highest for the LS-PMSM system without a gearbox or DMF. Changing to a HS-PMSM with a gearbox and a dual mass flywheel leads to a decrease of 2.1 percentage points to 2.5 percentage points in efficiency depending on the operating point. This data is based on a PMSM design, which is not optimally fitted to the investigated application. Therefore, it offers a poor efficiency for the high speed operating point. A tailor-made PMSM will provide a higher efficiency.

In contrast, the HS-PMSM system's higher reduced inertia decreases the speed fluctuations, and a DMF leads to a virtually uniform rotational speed on the generator side. Two aspects that have an influence on the acoustic behavior are studied: the decoupling is highly advantageous for eliminating gear rattle, but it also causes disadvantages concerning rolling torque.

For the optimal system design, a tradeoff including the design criteria efficiency, weight, packaging, and cost have to be weighted specifically for each application. The high-speed concept offers less efficiency in this study. However, weight and volume are decreased by 5.6 % and 11.6 % respectively. Therefore, the high-speed concept offers a higher power density, leading to reduced costs and eventually weight.

In range extender units, strong interdependencies of the subsystems are given. Some aspects like system efficiency, noise and vibrations, and system control can only be investigated reliably, if the total system is analyzed as a unit. The study has shown that multi-domain Co-Simulation is a suitable option for range extender system investigations.

Further research concerning the acoustic effects and the impact on weight, space, and cost are necessary to give a final design recommendation.

ACKNOWLEDGEMENT–Funded by the Deutsche Forschungsgemeinschaft (DFG, German Research Foundation) – GRK 1856. This work was partially performed within the "Center for Mobile Propulsion", which is funded by DFG. The authors would like to express their gratitude to Mr. Florian König for his valuable contributions.

REFERENCES

Andert, J., Herold, K., Savelsberg, R. and Pischinger, M. (2017). NVH optimization of range extender engines by electric torque profile shaping. *IEEE Trans. Control Systems Technology* **25**, **4**, 1465–1472.

Andert, J., Köhler, E., Niehues, J. and Schürmann, G. (2012). KSPG range extender – A new pathfinder to electromobility. *ATZautotechnology* **12**, **2**, 26–33.

Bassett, M., Hall, J., Cains, T. and Warth, M. (2012). Fahrzeugintegration eines range-extender-antriebs. *Motortechnische Zeitschrift* **73**, **11**, 852–856.

Bianchi, N., Bolognani, S. and Luise, F. (2003). Potentials and limits of high speed PM motors. *Proc. IEEE Conf. 38th IAS Annual Meeting, Industry Applications Conf.*, Salt Lake City, Utah, USA.

Borisavljevic, A., Polinder, H. and Ferreira, J. A. (2010). On the speed limits of permanent-magnet machines. *IEEE Trans. Industrial Electronics* **57**, **1**, 220–227.

Eberle, U. (2012). Chancen und herausforderungen der elektromobilität. *4th VDI Fachkongress Elektromobilität*, Nürtingen, Germany.

Finken, T., Hombitzer, M. and Hameyer, K. (2010). Study and comparison of several permanent-magnet excited rotor types regarding their applicability in electric vehicles. *Proc. IEEE Emobility - Electrical Power Train*, Leipzig, Germany.

Fischer, R., Fraidl, G. K., Hubmann, C., Kapus, P. E., Kunzemann, R., Sifferlinger, B. and Beste, F. (2009). Range-extender-modul: Wegbereiter für elektrische mobilität. *MTZ - Motortechnische Zeitschrift* **70**, **10**, 752–759.

Gebrehiwot, M. and van den Bossche, A. (2015). Starting requirements of a range extender for electric vehicles: Based on a small size 4-stroke engine. *Int. J. Automotive Technology* **16**, **4**, 707–713.

Grosse, T., Hameyer, K. and Hagedorn, J. (2014). Needle winding technology for symmetric distributed windings. *Proc. Conf. 4th Int. Electric Drives Production*, Nuremberg, Germany.

Heron, A. and Rinderknecht, F. (2013). Comparison of range extender technologies for battery electric vehicles. *Proc. IEEE 8th Int. Conf. and Exhibition Ecological*

Vehicles and Renewable Energies (EVER), Monte Carlo, Monaco.

Herrmann, M. and Matthé, R. (2014). Wege in die Elektromobilität – Empfehlungen aus Erfahrungen. *E-Motive: 6. Expertenforum Elektrische Fahrzeugantriebe*, Wolfsburg, Germany.

Karthaus, J., Steentjes, S., Gröbel, D., Andreas, K., Merklein, M. and Hameyer, K. (2017). Influence of the mechanical fatigue progress on the magnetic properties of electrical steel sheets. *Archives of Electrical Engineering* **66**, **2**, 351–360.

Köhler, J., Esch, H.-J., Niehues, J., Andert, J., Pischinger, M. and Schürmann, G. (2012). Engine test bench and vehicle testing of KSPG range extender "FEVcom" full engine vibration compensation. *21st Aachen Colloquium Automobile and Engine Technology*, Aachen, Germany.

Liu, Q. and Hameyer, K. (2016). A deep field weakening control for the PMSM applying a modified overmodulation strategy. *Proc. IEEE Conf. 8th IET Int. Conf. Power Electronics, Machines and Drives (PEMD 2016)*, Glasgow, UK.

Pischinger, M. and Andert, J. (2014). Generator Control System for Smooth Operation with Combusion Engine. Patent No. US 2014/0167423 A1.

Pischinger, R., Klell, M. and Sams, T. (2009). *Thermodynamik der Verbrennungskraftmaschine*. Der Fahrzeugantrieb. 3rd edn. Springer. Wien, Austria.

Reik, W., Seebacher, R. and Kooy, A. (1998). Dual mass flywheel. *6th Luk Symp*., 69–94.

Schröder, D. (2015). *Elektrische Antriebe – Regelung von Antriebssystemen*. 4th edn. Spriger-Verlag Berlin Heidelberg. Heidelberg, Germany.

Schröter, J., Hoffmann, M., Jacobs, G. and Straßburger, F. (2015). High speed electrical drives for mobile machinery: An approach for raising the efficiency of agriculture and construction machinery. *VDI-Berichte* **2251**, Düsseldorf, Germany, 71–76.

Schröter, J. and Jacobs, G. (2014). High speed electrical drives for mobile machinery – Drive concept and selected components. *Proc. Conf. 13th Int. CTI Symp. Automotive Transmissions, HEV and EV Drives*, Berlin, Germany.

Schröter, J., Jacobs, G., Zhitkova, S., Felden, M. and Hameyer, K. (2014). Development of high speed electrical drives for mobile machinery, challenges and potential solutions, challenges and potential solutions. *Proc. Conf. 9th Int. Fluid Power Conf*., Aachen, Germany.

Stier, C., Geier, M. and Albers, A. (2009). Analyse des drehzahleinflusses auf das dynamische übertragungsverhalten von ZMS. *Dynamisches Gesamtsystemverhalten von Fahrzeugantrieben*, Munich, Germany.

van Basshuysen, R. and Schäfer, F. (2015). *Handbuch Verbrennungsmotor: Grundlagen, Komponenten, Systeme, Perspektiven. ATZ/MTZ-Fachbuch.* 7th edn. Springer Vieweg. Wiesbaden, Germany.

Vibe, I. I. (1970). *Brennverlauf und Kreisprozess von Verbrennungsmotoren*. VEB Verlag Technik. Berlin, Germany.

Walter, A., Kiencke, U., Jones, S. and Winkler, T. (2007). Das zweimassenschwungrad als virtueller sensor: Echtzeitfähige rekonstruktion des direkt indizierten motor- und lastmoments. *Motortechnische Zeitschrift* **68**, **6**, 486–493.